

Chemically Resolved Interface Structure of Epitaxial Graphene on SiC(0001)

Jonathan D. Emery,¹ Blanka Detlefs,² Hunter J. Karmel,¹ Luke O. Nyakiti,³ D. Kurt Gaskill,³
Mark C. Hersam,^{1,4} Jörg Zegenhagen,² and Michael J. Bedzyk^{1,5,*}

¹*Department of Materials Science and Engineering, Northwestern University, Evanston, Illinois 60208, USA*

²*European Synchrotron Radiation Facility, BP 220, 38043 Grenoble, Cedex 9, France*

³*US Naval Research Laboratory, Washington, District of Columbia 20375, USA*

⁴*Department of Chemistry, Northwestern University, Evanston, Illinois 60208, USA*

⁵*Department of Physics and Astronomy, Northwestern University, Evanston, Illinois 60208, USA*

(Received 25 July 2013; published 19 November 2013)

Atomic-layer 2D crystals have unique properties that can be significantly modified through interaction with an underlying support. For epitaxial graphene on SiC(0001), the interface strongly influences the electronic properties of the overlying graphene. We demonstrate a novel combination of x-ray scattering and spectroscopy for studying the complexities of such a buried interface structure. This approach employs x-ray standing wave-excited photoelectron spectroscopy in conjunction with x-ray reflectivity to produce a highly resolved chemically sensitive atomic profile for the terminal substrate bilayers, interface, and graphene layers along the SiC[0001] direction.

DOI: [10.1103/PhysRevLett.111.215501](https://doi.org/10.1103/PhysRevLett.111.215501)

PACS numbers: 61.48.Gh, 61.05.cm, 68.49.Uv, 79.60.-i

Epitaxial graphene (EG) grown on the Si-terminated face of silicon carbide [SiC(0001)] is of interest due to its unique physical properties [1,2], potential in numerous applications [3–5], and amenity for wafer-scale fabrication [6,7]. EG/SiC(0001) production proceeds *via* preferential Si sublimation and reconstruction of the surface C to yield a heterostructure that exhibits the technologically relevant properties characteristic of graphene, such as the Dirac cone band structure [8,9] and large room-temperature Hall mobilities [1,6]. As such, EG/SiC(0001) is a comparatively viable option for the large-scale production of graphene. However, despite the advancement in both fundamental understanding and practical application of the material, there remains much unknown about the structure and behavior of EG/SiC(0001), particularly concerning the influence of the EG/SiC(0001) interface on the properties of the overlying graphene.

Early studies revealed that EG/SiC(0001) possesses a complex $6\sqrt{3} \times 6\sqrt{3}R30^\circ$ ($6R3$) reconstructed interfacial layer [10], referred to herein as the interfacial, or EG₀, layer. This layer has significant influence on the growth, morphology, and electronic behavior of the overlying graphene [8,11–14]. It has been contentiously debated as the cause of EG/SiC(0001) symmetry breaking and band gap opening [15,16], and has been identified as a primary source for carrier doping and scattering in the graphene layers [17,18]. Work on H-intercalated graphene transistors highlights the influence of this layer on the electronic properties of the overlying graphene, demonstrating that physically decoupling the EG₀ layer from the substrate improves properties critical to graphene-based transistor performance [19,20]. A precise understanding of the structure of EG/SiC(0001) is therefore not only fundamentally important, but is also central to the prospects of graphene engineering and functionalization.

Because of the importance of the interfacial layer to the behavior of EG/SiC(0001), there have been numerous efforts to characterize its structure, including low-energy electron diffraction [10,13], scanning-tunneling microscopy, [21–23], x-ray photoemission spectroscopy (XPS) [24,25], x-ray reflectivity (XRR) [26], and cross-sectional transmission electron microscopy [27,28]. These experimental reports, combined with computational studies [14,29,30], have generated a multitude of interfacial models. These include those with weak [10] or strong [12,14,25,29] substrate-interlayer coupling, C-rich [14,23,25] or Si-rich interfacial structures [21,26], or significant populations of Si dangling bonds [12,29]. However, despite this persistent incongruence, it is now understood that the interface consists of a corrugated, topologically graphenelike layer which, due to its coupling with the underlying SiC, lacks the electronic properties of pristine graphene [25,31].

In this Letter we detail the structure of the interface by employing a suite of x-ray characterization techniques, including depth-sensitive XPS, x-ray standing wave-enhanced XPS (XSW-XPS), and x-ray reflectivity (XRR). These tools, when employed collectively, provide the chemically specific structural information necessary to clarify previously unknown details of the EG/SiC(0001) interface. This approach ultimately enables the construction of a chemically resolved interfacial map with sub-Å resolution along the SiC[0001] direction.

The XSW technique affords conventional photoelectron spectroscopy with high spatial resolution due to the influence of the XSW [here produced by the SiC(0006) Bragg reflection] on the photoabsorption process. A depiction of this phenomenon is shown in Fig. 1. The XSW phase can be adjusted relative to the atomic planes by tuning the incident beam energy (E_γ) within the range of the Bragg reflection, which in turn modulates the x-ray photoelectron yields of

Report Documentation Page				Form Approved OMB No. 0704-0188	
Public reporting burden for the collection of information is estimated to average 1 hour per response, including the time for reviewing instructions, searching existing data sources, gathering and maintaining the data needed, and completing and reviewing the collection of information. Send comments regarding this burden estimate or any other aspect of this collection of information, including suggestions for reducing this burden, to Washington Headquarters Services, Directorate for Information Operations and Reports, 1215 Jefferson Davis Highway, Suite 1204, Arlington VA 22202-4302. Respondents should be aware that notwithstanding any other provision of law, no person shall be subject to a penalty for failing to comply with a collection of information if it does not display a currently valid OMB control number.					
1. REPORT DATE 19 NOV 2013		2. REPORT TYPE		3. DATES COVERED 00-00-2013 to 00-00-2013	
4. TITLE AND SUBTITLE Chemically Resolved Interface Structure of Epitaxial Graphene on SiC(0001)				5a. CONTRACT NUMBER	
				5b. GRANT NUMBER	
				5c. PROGRAM ELEMENT NUMBER	
6. AUTHOR(S)				5d. PROJECT NUMBER	
				5e. TASK NUMBER	
				5f. WORK UNIT NUMBER	
7. PERFORMING ORGANIZATION NAME(S) AND ADDRESS(ES) Northwestern University, Department of Materials Science and Engineering, Evanston, IL, 60208				8. PERFORMING ORGANIZATION REPORT NUMBER	
9. SPONSORING/MONITORING AGENCY NAME(S) AND ADDRESS(ES)				10. SPONSOR/MONITOR'S ACRONYM(S)	
				11. SPONSOR/MONITOR'S REPORT NUMBER(S)	
12. DISTRIBUTION/AVAILABILITY STATEMENT Approved for public release; distribution unlimited					
13. SUPPLEMENTARY NOTES					
14. ABSTRACT					
15. SUBJECT TERMS					
16. SECURITY CLASSIFICATION OF:			17. LIMITATION OF ABSTRACT Same as Report (SAR)	18. NUMBER OF PAGES 21	19a. NAME OF RESPONSIBLE PERSON
a. REPORT unclassified	b. ABSTRACT unclassified	c. THIS PAGE unclassified			

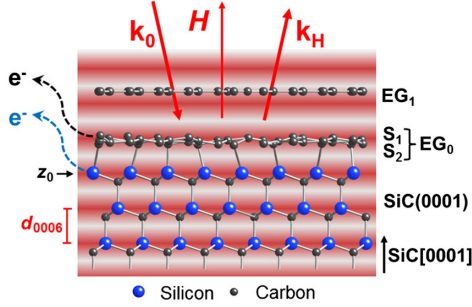


FIG. 1 (color online). Schematic of the XSW generated by the 6H-SiC(0006) Bragg reflection (period of $d = 2.52$ Å). The incident and reflected plane waves (wave vectors \mathbf{k}_0 and \mathbf{k}_H , respectively) interfere to produce a standing wavefield (antinodes shaded red).

atoms within the field. Depending on the spatial distribution of these atoms with respect to the substrate, this process produces distinct photoemission yield modulations as a function of E_γ . XSW data analysis determines two model-independent fit parameters, f_j and P_j , which are the amplitude and phase of the $H = 0006$ Fourier component of the j th chemically sensitive atomic density profile. For details, see the Supplemental Material [32] and Ref. [33].

In this work we will assume a normalized Gaussian distribution for each XPS-selected atomic layer. The (0006) Fourier component is therefore

$$F_j = f_j e^{2\pi i P_j} = e^{-2\pi^2 \sigma_j^2 / d^2} e^{2\pi i z_j / d}. \quad (1)$$

For this model, the XSW-measured Fourier amplitude f_j determines the Gaussian width σ_j , and the measured phase, $P_j = z_j / d$ ($0 \leq P_j < 1$), determines the mean height z_j (*modulo-d*) of the j th atomic layer relative to the substrate unit cell origin z_0 (Fig. 1). Because of the *modulo-d* ambiguity and potential contributions to P_j from multiple atomic layers, we supplement this analysis with high-resolution XRR (see Ref. [34] and references therein), a measurement that is sensitive to electron density distributions over a larger spatial extent.

EG/SiC(0001) samples of 1.3 and 0.5 monolayer (ML) of graphene = 38.2 C/nm² graphene coverage (Θ_T) were prepared by thermal decomposition of 6H-SiC(0001) substrates in ultrahigh vacuum (UHV) at 1200–1300 °C. Results for the 1.3 ML sample are presented in the main text. Complimentary analysis of the 0.5 ML sample, as well as an Ar-grown sample of 1.7 ML coverage, are provided in the Supplemental Material [32] to confirm and generalize the conclusions of the main text. Prior to measurements, the samples were annealed in UHV at ~ 600 °C, and the presence of the 6R3 interface was verified with low-energy electron diffraction. Further sample preparation details are provided in the Supplemental Material [32].

XSW-XPS measurements were performed in UHV at the ID32 beam line of the European Synchrotron Radiation Facility. Working near the SiC(0006) Bragg

back-reflection condition ($\theta_B \sim 88^\circ$), the incident beam energy and FWHM bandwidth were $E_\gamma = E_B = 2450$ and $\Delta E_\gamma = 0.34$ eV, respectively. The total FWHM resolution of the spectrometer was 0.6 eV. To vary the depth sensitivity, the photoemission angle (α) was set to either 78° or 2° , as shown in Fig. 2. The grazing ($\alpha = 2^\circ$) emission geometry was used during XSW experiments. XRR data were acquired at 5ID-C at the Advanced Photon Source. XRR integrated signal intensity was extracted following the methods described in Ref. [34]. XRR data fitting was limited to the region $1.2 < L < 14.0$, where $L = (c_{\text{SiC}} q_z) / (2\pi)$ is the SiC reciprocal lattice index, $q_z = 4\pi \sin(2\theta/2) / \lambda$ is the out-of-plane component of the momentum transfer vector, 2θ is the scattering angle, λ is the x-ray wavelength, and $c_{\text{SiC}} = 15.12$ Å is the lattice constant for 6H-SiC.

Figure 2 presents depth-sensitive (effective probing depth Λ_{eff}) core-level photoelectron spectra used to identify near-surface C and Si chemical species. When measured at emission angle $\alpha = 78^\circ$ [Figs. 2(a) and 2(b)], the Si 1s and C 1s spectra are dominated by bulk SiC components with binding energies (BE) of 1841.6 ± 0.1 and 283.8 ± 0.1 eV, respectively. The C 1s spectrum possesses additional high-energy core-shifted components from graphene and interfacial layers, as previously investigated [22,24,25]. The Si 1s spectrum, in contrast, appears to consist of a single component. By reducing α to 2° , Λ_{eff} is reduced from nm to Å scale [Figs. 2(c) and 2(d)]. A comparison of the C 1s spectra in Figs. 2(a) and 2(c) reveals strong attenuation ($\times 1/30$) of the C_{Bulk} integrated signal with respect to the higher BE spectral components.

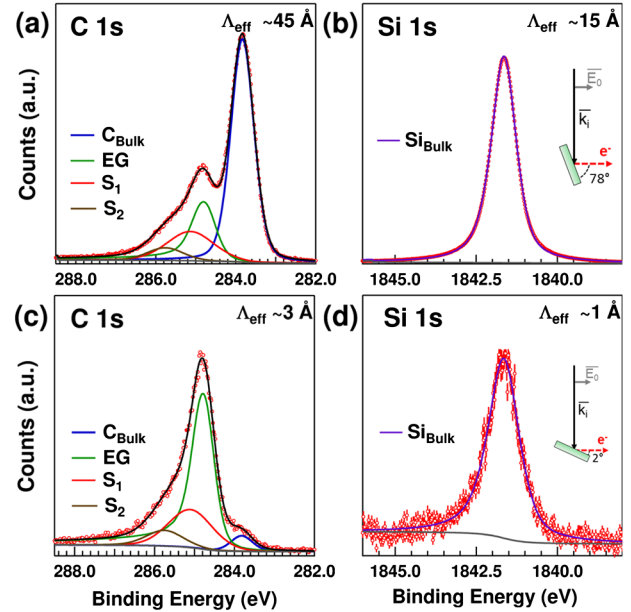


FIG. 2 (color online). C 1s and Si 1s photoelectron spectra for 1.3 ML EG/SiC(0001). Si_{Bulk} , C_{Bulk} , EG, S_1 , and S_2 components are shown in purple, blue, green, red, and brown, respectively. (a)–(b) Data collected at emission angle $\alpha = 78^\circ$. (c)–(d) Data collected with a highly surface-sensitive geometry ($\alpha = 2^\circ$).

In contrast, no distinguishable surface-specific component is present in the $\alpha = 2^\circ$ Si 1s spectrum [Fig. 2(d)].

We identify three distinct C 1s surface species, labeled in Figs. 2(a) and 2(c) as EG, S_1 , and S_2 . These components are shifted in BE by +0.95, +1.35, and +1.95 eV with respect to the C_{Bulk} peak, and have resolution-broadened FWHMs of 0.7, 1.0, and 1.1 eV. The EG component arises from the graphene layers, and the S_1 and S_2 components belong to species within the interfacial layer. The Si 1s spectra are fit with a single, slightly asymmetrically broadened line shape [Figs. 2(b) and 2(d)]. When the geometry is more highly surface sensitive the peak broadens by $\sim 20\%$, as would be consistent with the increased relative contribution of strained, near-surface Si-C bonds possessing a variety of bonding configurations due to interactions between terminal Si species and C within the interfacial layer.

Using the XPS peak-fitting models described above, we extract the chemically specific, E_γ -dependent XSW photoemission yields (Fig. 3). Each of the five measured components exhibits a distinct XSW modulation, demonstrating that each chemical species possesses a distinct distribution profile along the SiC[0001] direction. Results from least-squares fitting of the yield equation [32,33] to the data are overlaid for each component in Fig. 3. All best-fit f_j and P_j values are reported in Table I.

The Fourier phases for both Si_{Bulk} and C_{Bulk} indicate that these species are centered at their nominal SiC positions (equal to 0.00 and -0.25 , respectively). However, small deviations of XSW best-fit results for both species from the ideal Si_{Bulk} and C_{Bulk} values (-0.05 and $+0.05$ Å, respectively) imply the possibility of small displacements. The Fourier amplitude $f_{C_{\text{Bulk}}} = 1.0 \pm 0.1$ denotes essentially perfect C_{Bulk} coherency with the substrate. Conversely, the Si_{Bulk} result ($f_{\text{Si}_{\text{Bulk}}} = 0.8 \pm 0.1$) suggests a broader-than-ideal distribution for Si atoms within the topmost SiC

bilayers ($\sigma_{\text{Si}_{\text{Bulk}}} = 0.3 \pm 0.1$ Å, as compared to the bulk ~ 0.1 Å thermal vibrational amplitude for SiC at room temperature).

The results for the S_1 and S_2 components are shown in Fig. 3(b). Converted to absolute positions [Eq. (1)], the S_1 and S_2 components reside at $z_{S_1} = 2.39 \pm 0.13$ and $z_{S_2} = 2.07 \pm 0.10$ Å above the terminal Si layer. In addition, a comparison of the Fourier amplitudes of the interfacial species reveals a smaller value for S_1 , indicating that σ_{S_1} is significantly broader in comparison to σ_{S_2} .

The remaining C 1s component arises from atoms located in the EG overlayers. Because EG/SiC(0001) does not grow in a single, uniform monolayer [6], single-layer XSW modeling is inappropriate. Instead, the f_{EG} and P_{EG} values are determined from the superposition of contributions from $k > 1$ atomic layers of graphene. Here, the long-range structural information lacking in XSW is provided by XRR, thereby enabling the exploration of models with varying EG layer coverage.

XRR data are analyzed by comparing measured reflectivity values to those calculated from a model consisting of k atomic layers, each described by layer occupancy (Θ_k), position (z_k), and distribution width (σ_k) [26,34]. In this work, we are able to constrain the XRR analysis using XSW results (within 1-sigma confidence levels), thereby mitigating ambiguities that commonly arise during model-based XRR fitting. For Si_{Bulk} and C_{Bulk} , we allow for the slight broadening and displacement of bulk-positioned atoms within the three topmost SiC bilayers. Importantly, XSW interpretation of the S_1 and S_2 signals constrains these two components into single, well-defined interfacial distributions.

The XSW-constrained XRR result is shown in Fig. 4(a). The fit finds the EG₁, EG₂, and EG₃ layers positioned at 5.82, 9.17, and 12.57 Å above the terminal Si layer with respective coverages (Θ_k) of 0.86, 0.45, and 0.03 ML. The widths of the graphene layers (Table I), monotonically decrease as a function of distance from the interface, in close agreement with trends observed in Refs. [13,26]. The S_1 and S_2 layer positions converge to $z_{S_1} = 2.45$ and

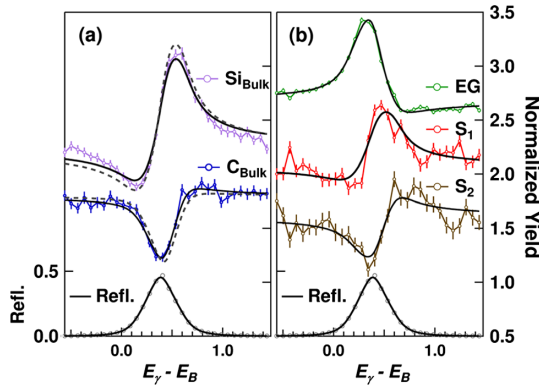


FIG. 3 (color online). XSW results for (a) near-surface bulk and (b) surface species corresponding to XPS components in Figs. 2(c) and 2(d). Measured (gray circles) and fitted (black) reflectivity from the SiC(0006) Bragg peak are plotted vs energy offset from the geometrical Bragg condition ($E_B = 2450$ eV). Normalized yields and best-fit results (black) are offset for clarity, and simulated yields for ideal SiC bulk are in dashed black.

TABLE I. XSW-measured values, P_j and f_j , for the j th chemical species. The absolute positions (z_j), widths (σ_j), and coverages (Θ_j) are derived using combined x-ray analysis. Uncertainties on the last significant figures are reported in parentheses.

j	P_j	$z_j(\text{\AA})$	f_j	$\sigma_j(\text{\AA})$	$^a\Theta_j(\text{MLs})$
EG $\begin{cases} \text{EG}_3 \\ \text{EG}_2 \\ \text{EG}_1 \end{cases}$	0.42(2)	12.57	0.48(5)	0.05	0.03
		9.16		0.11	0.45
		5.82		0.21	0.86
S_1	0.95(5)	2.4(1)	0.4(2)	0.5(1)	0.70
S_2	0.82(4)	2.1(1)	0.9(2)	0.2(1)	0.27
Si_{Bulk}	$-0.02(2)$	$-0.05(5)$	0.8(1)	0.3(1)	0.28
C_{Bulk}	$-0.23(2)$	$-0.58(5)$	1.0(1)	0.1(1)	0.34

^aBased on EG, 1 ML = 38.2 atoms/nm².

$z_{S_2} = 2.13 \text{ \AA}$, respectively, well within the 1-sigma confidence levels derived from XSW analysis. The topmost bulk Si layer is $\sim 15\%$ depleted, which is presumably a growth artifact from the Si sublimation and corroborates the observation of near-surface Si vacancies [35]. This Si depletion limits the maximum number of sp^3 -hybridized C atoms to $\sim 25\%$ of the atoms within the graphenelike interfacial layer. Finally, the C atoms in the topmost SiC bilayers are found to relax outward by, on average, 0.04 \AA , consistent with the XSW result ($0.05 \pm 0.05 \text{ \AA}$). With these results it is possible to compute the XRR-derived complex (0006) geometrical structure factor for the EG layers,

$$S_{EG} = \frac{1}{\Theta_T} \sum_{k=1}^3 \Theta_k e^{2\pi i z_k/d} e^{-2\pi^2 \sigma_k^2/d^2}, \quad (2)$$

and thereby back-calculate the amplitude, $f_{EG} = |S_{EG}| = 0.49$ and phase, $P_{EG} = \text{Arg}(S_{EG})/2\pi = 0.41$. These XRR values match closely with the XSW-derived values for EG, a testament to the exactitude and self-consistency of the model and analysis.

The resultant chemically sensitive atomic density profile $[N_a(z)]$ is shown in Fig. 4(b), and interfacial region detail is shown in Fig. 4(c). From this construction we conclude that the interfacial region contains a broad, C-only layer with graphenelike ($0.97 \pm 0.05 \text{ ML}$) atomic density. Within this layer there exist two chemically distinct C species. The S_2 species, which has the highest BE [Fig. 2(c)], accounts for $\sim 25\%$ of the interfacial C and is located $2.1 \pm 0.1 \text{ \AA}$ above the terminal Si layer. This displacement is only 0.2 \AA larger than the nominal Si-C bond distance of 1.9 \AA in SiC, indicating the partial sp^3 hybridization of the interfacial layer with substrate. The narrower distribution width of the S_2 species ($\sigma_{S_2} = 0.2 \pm 0.1 \text{ \AA}$) closely agrees with that of the topmost Si layer ($0.3 \pm 0.1 \text{ \AA}$), suggesting strong

coherency between the two layers. Furthermore, the coverage ratio for the topmost Si layer to S_2 is $\sim 1:1$ (Table I). These findings imply that each Si atom in the topmost SiC bilayer is chemically bonded to an interfacial S_2 atom and substantiates the claim that there exist essentially no unsaturated Si dangling bonds at the interface [25].

The S_1 species, which accounts for the other 75% of the interfacial C, is positioned $2.4 \pm 0.1 \text{ \AA}$ above the topmost Si layer and possesses a significantly larger distribution width ($\sigma_{S_1} \sim 0.5 \text{ \AA}$) as compared to the S_2 species. This broadening reduces the maximum areal density at the center of the interfacial layer and is consistent with the observations of a highly corrugated interfacial layer [2,14,22,30] as well as the reduced effective interfacial atomic density, as seen with cross-sectional transmission electron microscopy [27,28]. This broadening also points to multiple degrees of strain in the bonding configurations for the S_1 carbons, which is consistent with our finding of a slightly broader spectral width for the fitted S_1 XPS peak [32].

Our analysis yields no evidence for a number of other proposed interfacial structures. Specifically, Refs. [21,26] suggest the presence of large populations of interfacial Si atoms. These models prove inconsistent with our combined x-ray analysis. First, we find no spectroscopic evidence of nonbulk Si species, particularly from Si tetramers or other Si adatoms, which would exhibit negatively core-shifted Si $1s$ components with respect to the SiC signal due to the presence of Si-Si bonds. Instead, the depletion of Si in the topmost SiC bilayers suggests the presence of negatively charged Si vacancies [36], which may play a role in the n -type doping of the graphene layers. With respect to the difference in interpretation of the XRR presented herein and that of Ref. [26], we note that, because model-based fitting of XRR data often leads to numerous statistically equivalent solutions, unambiguous analysis typically requires complimentary information. Our approach benefits from constraints provided by the structurally sensitive XSW-XPS measurement and finds that the XRR data can be well fit with a C-only interfacial layer with graphenelike density, therefore generally supporting the models of Emtsev [25], Kim [14], and Varchon [30]. With respect to the discrepancy in XPS peak fitting between this work and that of Ref. [25], we note the following: (i) the model in Ref. [25] does not account for the probable existence of sub-ML EG inclusions in their nominally zero-layer graphene, and (ii) there are a large number of potential influences (e.g., bond-charge transfer, spontaneous substrate polarization [17], defect states [23], charge-transfer doping [25], band bending [19], and sp^2 vs sp^3 hybridization) on the precise binding energies of the interfacial species, making the identification of chemical species from peak shifts alone tenuous. Regardless, the binding energies that we find for S_1 ($=\text{BE}_{EG} + 0.4 \text{ eV}$) and S_2 ($=\text{BE}_{EG} + 1.0 \text{ eV}$) are in accordance with those expected from sp^2 - and sp^3 -hybridized species, respectively, and are strongly supported by XSW analysis.

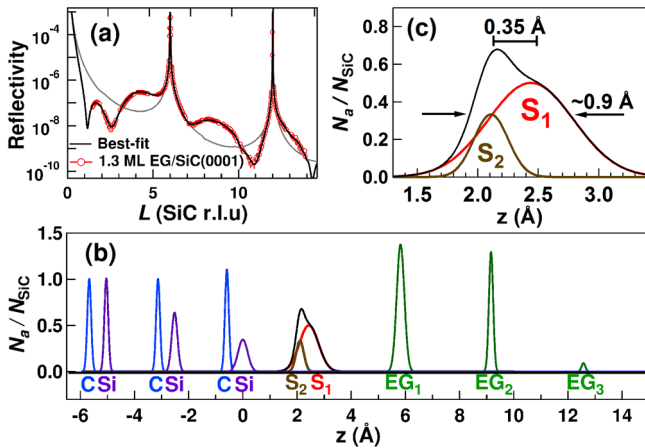


FIG. 4 (color online). (a) XSW-constrained x-ray reflectivity results for 1.3 ML EG/SiC(0001). The best fit (black) to the data (red) is shown together with a simulated bulk-truncated SiC curve (gray). (b) The atomic density map derived from combined XSW-XPS and XRR analysis. (c) The interfacial detail shows two interfacial components, S_1 and S_2 , separated by $\sim 0.35 \text{ \AA}$, to form a $\sim 0.9 \text{ \AA}$ wide, low-areal density interface layer.

In summary, we have combined depth-sensitive XPS, XSW-XPS, and XRR to create a structural profile of the EG/SiC(0001) interface with unprecedented chemical and spatial resolution. The high degree of consistency between the two sub-Å resolution measurements provides compelling evidence for the validity of our structural model and overall methodology. The interfacial layer, which has an influential role in the electronic behavior of EG/SiC(0001), and, consequently, in graphene-based devices, consists solely of C, possessing two distinct chemical species located at 2.1 and 2.4 Å above the topmost Si layer of the SiC. Our results support the strongly interacting interfacial layer model and rule out any significant presence of Si species in adatom structures or within the interfacial layer. In perspective, XSW-XPS and XRR may prove an effective tool for the study of the complex interfaces that exist in emerging 2D crystals and heterostructures, including intercalated, doped, and functionalized EG/SiC nanostructures.

We acknowledge support from MRSEC (NSF Grant No. DMR-1121262) and the Office of Naval Research for the support of the NRL, H.J.K., and M.C.H. through Grant No. N00014-11-1-0463. M.C.H. also acknowledges the Keck Foundation. We acknowledge use of ID32, ESRF, and DND-CAT, APS (DOE Award No. DE-AC02-06CH11357 to ANL). DND-CAT is supported by DuPont, Northwestern University, and Dow. We acknowledge use of X24A at NSLS (DOE Award No. DE-AC02-98CH10886 to BNL) for initial XSW measurements with assistance from Joseph Woicik (NIST). We acknowledge Denis Keane (DND-CAT) and Paul Fenter (ANL) for assistance with XRR measurements, Chip Eddy (NRL) for useful discussions on graphene synthesis, and Virginia Wheeler and Rachael Myers-Ward (NRL) for sample production.

*Corresponding author.

bedzyk@northwestern.edu

- [1] C. Berger *et al.*, *J. Phys. Chem. B* **108**, 19912 (2004).
- [2] C. Berger *et al.*, *Science* **312**, 1191 (2006).
- [3] Y.-M. Lin, C. Dimitrakopoulos, K. A. Jenkins, D. B. Farmer, H.-Y. Chiu, A. Grill, and P. Avouris, *Science* **327**, 662 (2010).
- [4] Y.-M. Lin *et al.*, *Science* **332**, 1294 (2011).
- [5] A. Tzalenchuk, S. Lara-Avila, A. Kalaboukhov, S. Paolillo, M. Syväjärvi, R. Yakimova, O. Kazakova, T. Janssen, V. Fal'Ko, and S. Kubatkin, *Nat. Nanotechnol.* **5**, 186 (2010).
- [6] K. V. Emtsev *et al.*, *Nat. Mater.* **8**, 203 (2009).
- [7] Y.-M. Lin, A. Valdes-Garcia, S.-J. Han, D. B. Farmer, I. Meric, Y. Sun, Y. Wu, C. Dimitrakopoulos, A. Grill, and P. Avouris, *Science* **332**, 1294 (2011).
- [8] T. Ohta, A. Bostwick, J. L. McChesney, T. Seyller, K. Horn, and E. Rotenberg, *Phys. Rev. Lett.* **98**, 206802 (2007).
- [9] S. Zhou, G.-H. Gweon, J. Graf, A. Fedorov, C. Spataru, R. Diehl, Y. Kopelevich, D.-H. Lee, S. G. Louie, and A. Lanzara, *Nat. Phys.* **2**, 595 (2006).
- [10] A. J. Van Bommel, J. E. Crombeen, A. Van Tooren, *Surf. Sci.* **48**, 463 (1975).
- [11] A. Bostwick, T. Ohta, T. Seyller, K. Horn, and E. Rotenberg, *Nat. Phys.* **3**, 36 (2006).
- [12] F. Varchon *et al.*, *Phys. Rev. Lett.* **99**, 125805 (2007).
- [13] C. Riedl, U. Starke, J. Bernhardt, M. Franke, and K. Heinz, *Phys. Rev. B* **76**, 374009 (2007).
- [14] S. Kim, J. Ihm, H. J. Choi, and Y. W. Son, *Phys. Rev. Lett.* **100**, 176802 (2008).
- [15] S. Y. Zhou, G. H. Gweon, A. V. Fedorov, P. N. First, W. A. De Heer, D. H. Lee, F. Guinea, A. H. C. Neto, and A. Lanzara, *Nat. Mater.* **6**, 916 (2007).
- [16] E. Rotenberg, A. Bostwick, T. Ohta, J. L. McChesney, T. Seyller, and K. Horn, *Nat. Mater.* **7**, 258 (2008).
- [17] J. Ristein, S. Mammadov, and T. Seyller, *Phys. Rev. Lett.* **108**, 246104 (2012).
- [18] G. M. Rutter, J. N. Crain, N. P. Guisinger, T. Li, P. N. First, and J. A. Stroscio, *Science* **317**, 219 (2007).
- [19] C. Riedl, C. Coletti, T. Iwasaki, A. A. Zakharov, and U. Starke, *Phys. Rev. Lett.* **103**, 246804 (2009).
- [20] J. A. Robinson, M. Hollander, M. LaBella, K. A. Trumbull, R. Cavalero, and D. W. Snyder, *Nano Lett.* **11**, 3875 (2011).
- [21] G. M. Rutter, N. P. Guisinger, J. N. Crain, E. A. A. Jarvis, M. D. Stiles, T. Li, P. N. First, and J. A. Stroscio, *Phys. Rev. B* **76**, 235416 (2007).
- [22] W. Chen, H. Xu, L. Liu, X. Y. Gao, D. C. Qi, G. W. Peng, S. C. Tan, Y. P. Feng, K. P. Loh, and A. T. S. Wee, *Surf. Sci.* **596**, 176 (2005).
- [23] Y. Qi, S. H. Rhim, G. F. Sun, M. Weinert, and L. Li, *Phys. Rev. Lett.* **105**, 085502 (2010).
- [24] L. I. Johansson, F. Owman, and P. Martensson, *Phys. Rev. B* **53**, 13 793 (1996).
- [25] K. V. Emtsev, F. Speck, T. Seyller, L. Ley, and J. D. Riley, *Phys. Rev. B* **77**, 155303 (2008).
- [26] J. Hass, J. E. Millan-Otoya, P. N. First, and E. H. Conrad, *Phys. Rev. B* **78**, 205424 (2008).
- [27] J. Borysiuk, R. Bozek, W. Strupinski, A. Wyszynski, K. Grodecki, R. Steapniewski, and J. M. Baranowski, *J. Appl. Phys.* **105**, 023503 (2009).
- [28] X. J. Weng, J. A. Robinson, K. Trumbull, R. Cavalero, M. A. Fanton, and D. Snyder, *Appl. Phys. Lett.* **97**, 201905 (2010).
- [29] A. Mattausch and O. Pankratov, *Phys. Rev. Lett.* **99**, 076802 (2007).
- [30] F. Varchon, P. Mallet, J. Y. Veuillen, and L. Magaud, *Phys. Rev. B* **77**, 235412 (2008).
- [31] S. Goler *et al.*, *Carbon* **51**, 249 (2013).
- [32] See Supplemental Material at <http://link.aps.org/supplemental/10.1103/PhysRevLett.111.215501> for supporting data and details on XSW and XPS modeling, sample preparation, experimental procedures, and analysis of complimentary samples.
- [33] D. P. Woodruff, *Rep. Prog. Phys.* **68**, 743 (2005).
- [34] J. D. Emery, Q. H. Wang, M. Zarrouati, P. Fenter, M. C. Hersam, and M. J. Bedzyk, *Surf. Sci.* **605**, 1685 (2011).
- [35] X. Gao, S. Chen, T. Liu, W. Chen, A. T. S. Wee, T. Nomoto, S. Yagi, K. Soda, and J. Yuhara, *Phys. Rev. B* **78**, 201404 (2008).
- [36] T. Wimbauer, B. K. Meyer, A. Hofstaetter, A. Scharmann, and H. Overhof, *Phys. Rev. B* **56**, 7384 (1997).

Supplemental Material

Chemically Resolved Interface Structure of Epitaxial Graphene on SiC(0001)

Jonathan D. Emery¹, Blanka Detlefs², Hunter J. Karmel¹, Luke O. Nyakiti³, D. Kurt Gaskill³, Mark C. Hersam^{1,4}, Jörg Zegenhagen², Michael J. Bedzyk^{1,5}

1. Department of Materials Science and Engineering, Northwestern University, Evanston, Illinois 60208, USA

2. European Synchrotron Radiation Facility, BP 220, 38043, Grenoble, Cedex 9, France.

3. US Naval Research Lab, Washington, District of Columbia 20375, USA

4. Department of Chemistry, Northwestern University, Evanston Illinois, 60208, USA

5. Department of Physics and Astronomy, Northwestern University, Evanston Illinois, 60208, USA

X-ray Standing Wave

In the dipole approximation for the photoelectric effect, the normalized E_γ -dependent photoelectron yield is:

$$Y_j(E_\gamma) = 1 + R(E_\gamma) + 2p\sqrt{R(E_\gamma)}f_j\cos[\phi(E_\gamma) - 2\pi P_j], \quad (\text{S1})$$

where R is the Bragg reflectivity, E_γ is the incident photon energy, p is the polarization factor, and ϕ is the XSW phase. By fitting Eq. S1 to the photoelectron yield data from an atomic species with a specific chemical state, j , one can extract the Fourier amplitude and phase f_j and P_j to resolve the chemically sensitive atomic density profile, $N_j(z)$, which is defined in the main text (Eq. 1).

Experimental:

The 0.5 and 1.3 ML samples were grown from nominally on-axis nitrogen-doped 6H-SiC(0001) substrates graphitized by direct current flashing in UHV. The 0.5 ML sample was processed with a 550° C overnight degas followed by sequential flashes of 1000° C for 5 minutes, 1100° C for 5 minutes and 1200° C for 1 minute. The 1.3 ML sample was processed using the same degas and

1000° C and 1100° C anneals, but were treated with additional anneals at 1200° C, 1250° C, and 1300° C for 2, 2, and 1 minute, respectively.

EG synthesis of the 1.7 ML sample was carried out in a commercial hot-wall Aixtron/Epigress VP508 chemical vapor deposition reactor. Prior to graphene growth, substrates underwent an *in situ* H₂ etch at 1520°C for 30 minutes. After etching, H₂ was purged, and the subsequent EG formation process was conducted under a flowing Ar ambient of 10 standard liters per minute at 100 mbar at 1540° C for 30 minutes.

XSW-XPS measurements were performed in UHV (1×10^{-10} Torr) at the ID32 beam line[1] of the European Synchrotron Radiation Facility. The incident photon energy, E_γ , was set near the SiC(0006) back-reflection condition (Bragg angle, $\theta_B \sim 88^\circ$ and $E_\gamma \sim 2.450$ keV) using a Si(111) double crystal monochromator. The photon flux at the sample surface was 10^{12} photons/s within a 0.1×0.4 mm² spot size. Photoelectrons were collected with a SPECS-PHOIBOS 225 electron analyzer positioned with analyzer axis mounted parallel to the X-ray polarization

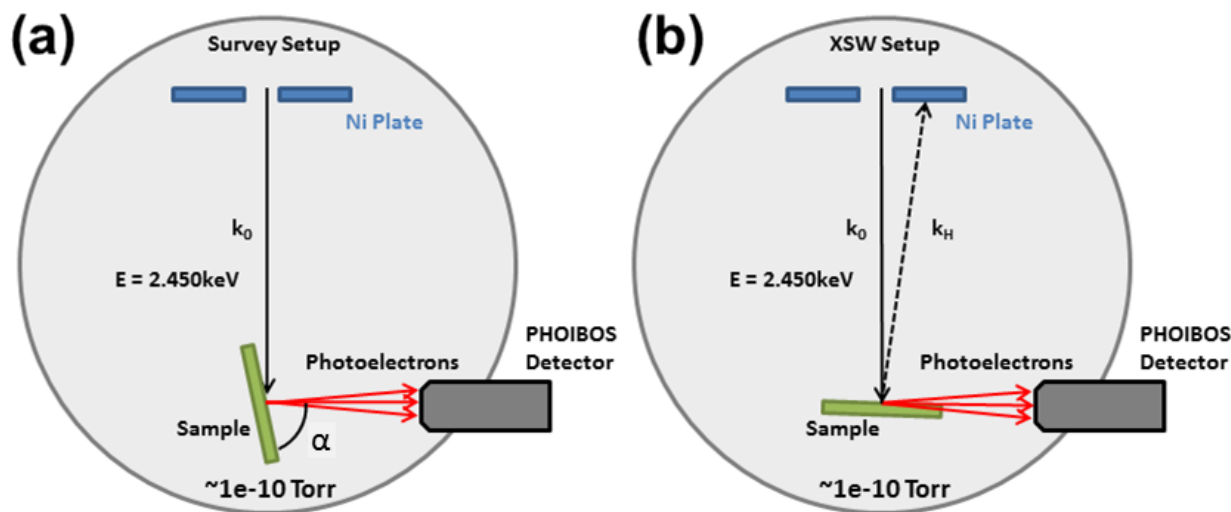


FIG. S1: Experimental geometries for both (a) conventional XPS ($\alpha \sim 78^\circ$) used for survey scans and (b) highly surface-sensitive grazing-emission XPS ($\alpha \sim 2^\circ$) used for XSW measurements. Tuning the emission angle to $\alpha \sim 2^\circ$ improves surface sensitivity by effectively decreasing the sampling depth of the photoelectrons originating from deep within the crystal as compared to those nearer to the surface. The effective sampling depth is $\Lambda_e \sim \text{IMFP} \sin(\alpha)$

LEED:

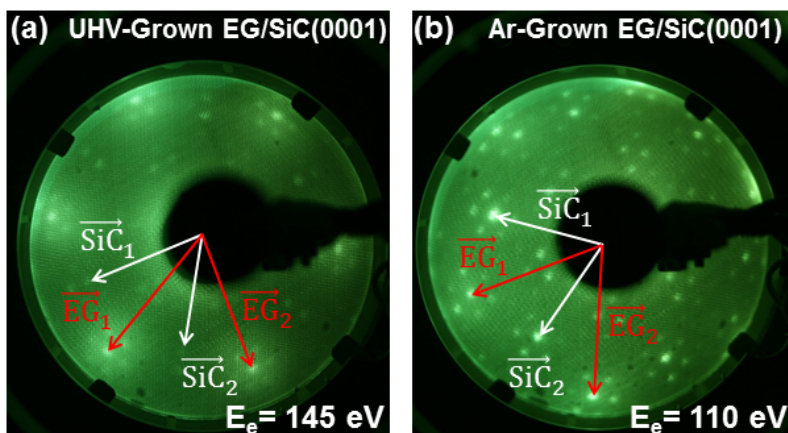


FIG. S2: LEED patterns for both 1.3 ML UHV-grown (a) and 1.7 ML Ar-grown (b) EG/SiC(0001). Each image shows the typical pattern with bright 1×1 EG (red arrow) and 1×1 SiC (white arrow) spots. The spots arranged in a hexagon about the EG spots are due to the $6\sqrt{3} \times 6\sqrt{3}$ $R30^\circ$ reconstructed interfacial layer. Ar-growth resulted in larger surface domains, subsequently resulting in the sharper LEED pattern in (b).

XPS Survey:

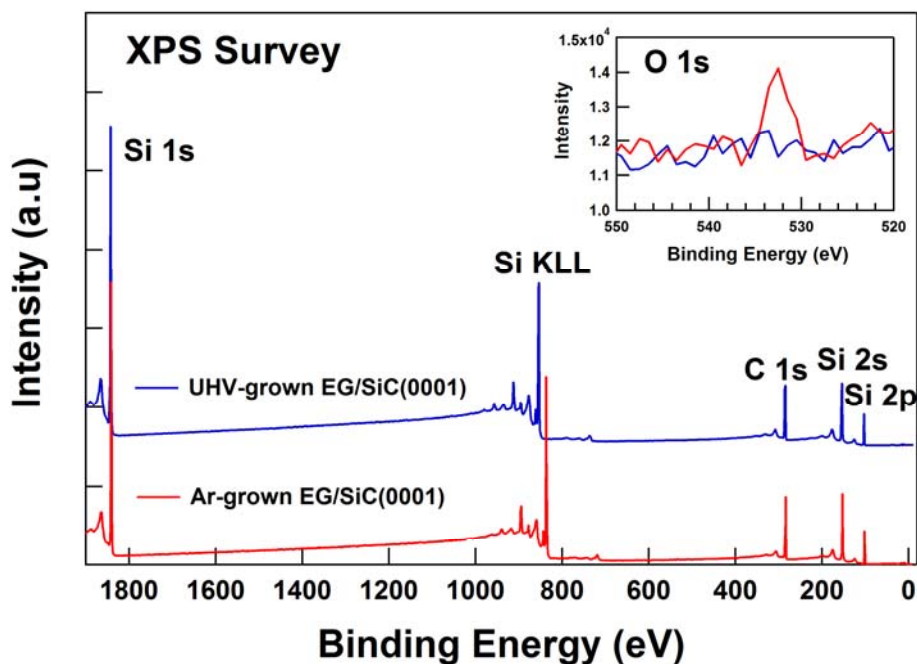


Figure S3: Survey spectra for 1.3 ML UHV-grown EG/SiC(0001) (blue) and 1.7 ML Ar-grown EG/SiC(0001) (red). Spectra were acquired with a photoemission angle $\alpha \sim 78^\circ$ (Fig. S1(a)) and using incident beam energies of 2.450 and 2.465 keV, respectively. The inset shows a weak O 1s signal present in the Ar-grown spectrum associated with a small amount of silicon oxide near-surface contamination. Oxide surface contamination is estimated in the text.

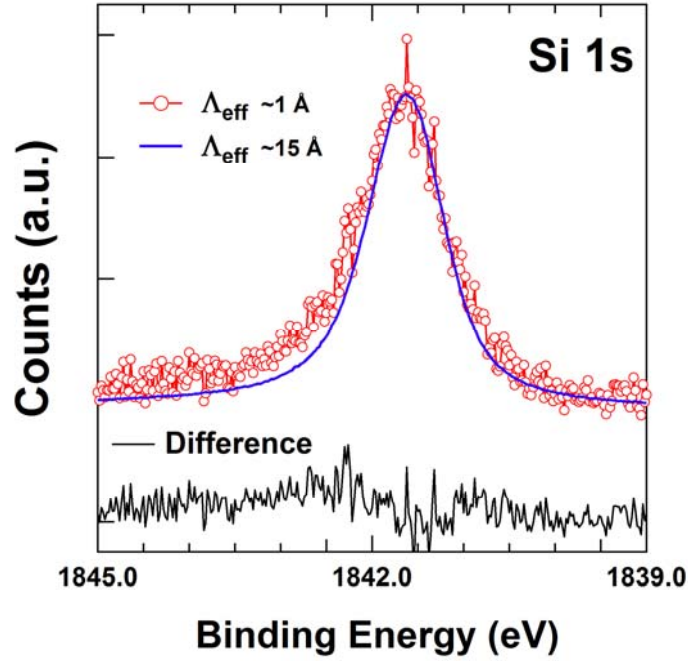


FIG. S4: Overlay of Si 1s spectra from 1.3 ML UHV-grown EG/SiC(0001) taken at emission angles $\alpha \sim 78^\circ$ (blue) and $\alpha \sim 2^\circ$ (red). The peak width broadens by $\sim 20\%$ when measured using the $\alpha = 2^\circ$ geometry, indicating increased spectral contribution from strained surface Si species. The difference trace is shown in black.

direction in order to minimize the influence of non-dipole contributions to the photoelectron yield [2, 3]. The FWHM total energy resolution of the photoelectron spectra was ~ 0.60 eV, which accounts for the FWHM incident beam bandwidth of 0.34 eV.

X-ray reflectivity measurements were performed in ambient at the Advanced Photon Source, Dupont-Northwestern-Dow Collaborative Access Team 5ID-C station using $E_\gamma = 17.0$ keV X-rays collimated to a 0.1×2.0 mm² spot size with a flux of $\sim 5 \times 10^{11}$ photons/s. The reflected intensity at the specular condition was measured using an area detector [4, 5]. Below $q_z \sim 0.5$ Å⁻¹, the finite surface domain size of UHV-grown samples resulted in significant transverse broadening of the specular rod, which inhibited accurate integration of the XRR signal.

Peak Fitting:

For all samples, the C_{Bulk} , S_1 and S_2 peaks are fit using either pseudo-Voigt functions or with a summation of Gaussian and Lorentzian lineshapes (SGL):

$$SGL(x; \gamma, x_0, \eta) = (1 - \eta) \text{Exp}[-4 \ln 2 \left(\frac{x - x_0}{F} \right)^2] + \eta \left(\frac{1}{1 + 4 \left(\frac{x - x_0}{F} \right)^2} \right) \quad \text{Eq. S1}$$

where the components are weighted by factor η and have common positions x_0 , and widths F . To account for the slight asymmetry in the Si 1s peak, we used a modified a -SGL function [6]. To account for the metallic nature of the EG, the peak is fit with a Gaussian-broadened Doniach-Sunjc [7] profile (DS):

Table S1: Fitting parameters for C 1s and Si 1s spectra from EG/SiC(0001) samples. SGL denotes a summation Gaussian-Lorentzian, a -SGL denotes an asymmetric SGL, with asymmetry factors a and b . DS represents a Doniach-Sunjc curve with asymmetry factor ϵ .

0.5 ML UHV-grown EG/SiC(0001)						
	Si 1s		C 1s			
Component	Bulk Si	SiO _x	Bulk C	EG	S ₁	S ₂
Lineshape	a -SGL	SGL	SGL	DS	SGL	SGL
ϵ or a/b	0.25,0.09	-	-	0.105	-	-
η	0.55	0.25	0.20	-	0.10	0.20
E _B	1841.70	1844.40	283.80	284.80	285.15	285.75
FWHM	1.25	2.05	0.85	0.70	1.15	1.00
1.3 ML UHV-grown EG/SiC(0001)						
	Si 1s		C 1s			
Component	Bulk Si	SiO _x	Bulk C	EG	S ₁	S ₂
Lineshape	a -SGL	SGL	SGL	DS	SGL	SGL
ϵ or a/b	0.25,0.09	-	-	0.105	-	-
η	0.55	-	0.20	-	0.10	0.20
E _B (eV)	1841.65	-	283.80	284.75	285.10	285.75
FWHM (eV)	1.12	-	0.90	0.70	1.1	1.0
1.7 ML Furnace-grown EG/SiC(0001)						
	Si 1s		C 1s			
Component	Bulk Si	SiO _x	Bulk C	EG	S ₁	S ₂
Lineshape	a -SGL	SGL	SGL	DS	SGL	SGL
ϵ or a/b	0.25,0.09	-	-	0.105	-	-
η	0.55	0	0.20	-	0.10	0.20
E _B (eV)	1841.65	1844.10	283.90	284.80	285.10	285.75
FWHM (eV)	1.1	1.95	0.85	0.64	1.0	0.9

$$DS(x: \varepsilon, f, x_0) = \frac{\cos\left[\frac{\pi\varepsilon}{2} + (1 - \varepsilon)\tan^{-1}\left(\frac{x - x_0}{F}\right)\right]}{[F^2 + (x - x_0)^2]^{(1-\varepsilon)/2}}, \quad \text{Eq. S2}$$

with asymmetry factor ε , position x_0 , and width F .

All spectra were fit using a Shirley background [8]. The asymmetry value ε for the EG peak was set to 0.105, consistent with observations from EG from H-intercalated EG/SiC(0001) [9]. Fit parameters for the spectra in Fig. 1 and S8 are provided in Table S1.

XSW Analysis Using Conventional C 1s and Si 1s Peak-fitting Models.

The peak-fitting models used to analyze the data in the main text (and summarized in Table S1) differ substantially from those typically employed [10, 11]. However, we note that the C 1s data from nominally zero-layer graphene presented in Ref. [10] can be well fit by accounting for a small amount of graphene coverage and inverting the $S_1:S_2$ intensity ratio (Fig. S5). The presence of such graphene inclusions on step edges have been thus far unavoidable during the production of nominally zero-layer graphene, and are observed even on the highest-quality samples grown using state-of-the-art processes in Ar atmosphere [12-14]. We also observe that the data presented in the Ref. [10] was acquired prior to the development of more well-controlled, homogenous EG/SiC(0001) produced by Ar anneal [15], increasing the likelihood of relatively high EG coverage on the samples presented in that work. It is therefore likely that the spectra presented in Ref. [10] should be fit accounting for contributions from EG layers, as is presented in Fig. S5.

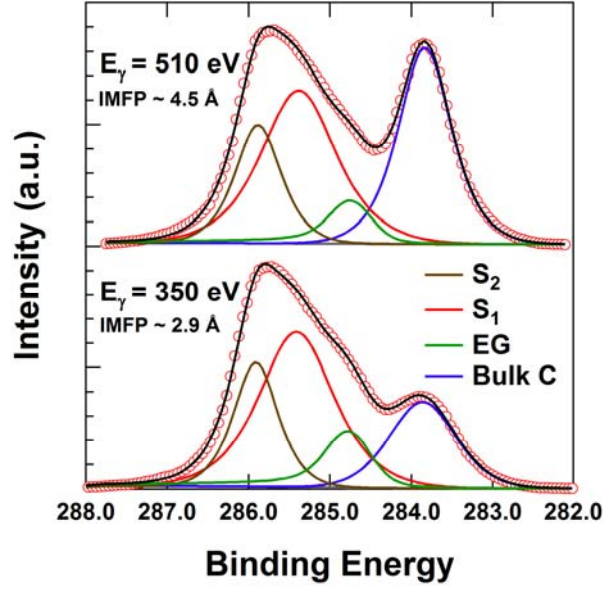


FIG. S5: Fits to data from nominal zero-layer graphene on SiC(0001) from Ref. [10], with C_{Bulk} , EG, S_1 , and S_2 components in blue, green, red, and brown, respectively. The spectra are fit accounting for a $\sim 15\%$ coverage of EG. In contrast to Ref. [10], the $S_1:S_2$ peak intensity ratio is essentially inverted.

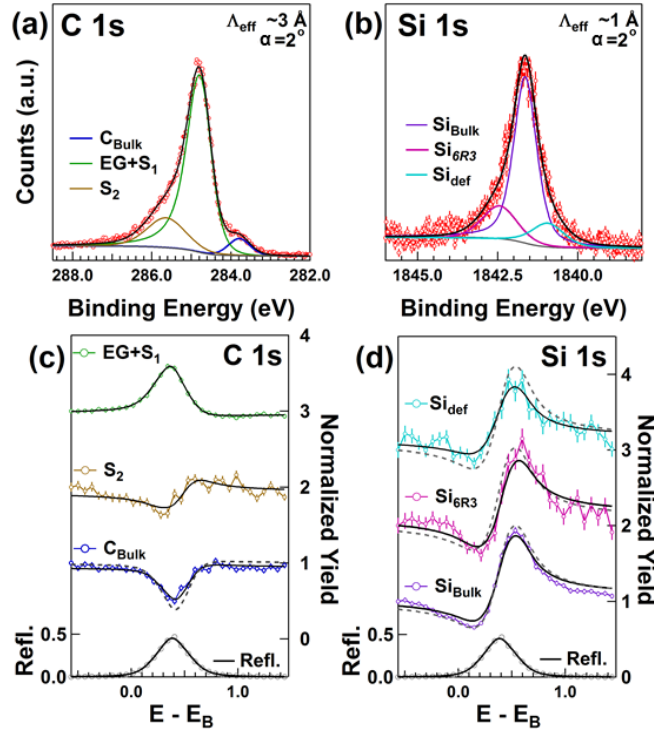


FIG. S6: XPS peak-fitting and subsequent XSW data using the fit parameters suggested by Emtsev *et al.* and Riedl. The data presented in these figures are the same as that presented in Figs. 2(c) and (d). (a) The C 1s data were fit with three peaks for XSW analysis because the S_1 and EG peaks were statistically inseparable. (b) The Si 1s peak fitting model shown here accounts for the possible presence of distinct 6R3 and defect related core-shifted components. In (c) and (d) the XSW results corresponding to the peak fitting models in (a) and (b), respectively. XPS yield curves are offset on the y-axis for clarity.

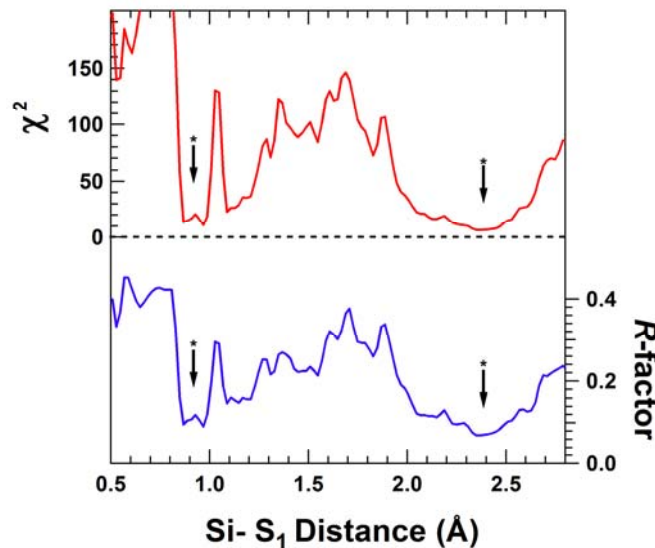


Figure S7: Goodness-of-fit maps for the Si-S₁ distance with fixed S₂ position using traditional [10] peak-fitting models. There exist two local minima, indicating possible solutions at Si-S₁ = 0.9 Å, and Si-S₁ = 2.4 Å, but both solutions lack realistic physical interpretation.

Similarly, Riedl *et al.* propose that the Si 2p spectrum be fit with a 3-peak model due to the presence of *6R3* and “defect” species [11]. We note, however, that even a moderate population of surface-specific species would presumably dominate the spectrum in a fashion similar to that observed for the C 1s spectrum, while the observed increase in the relative intensity on the wings of the Si 1s peak are marginal ($\sim \times 3$) when the measurement taken in the $\alpha \sim 2^\circ$ geometry as compared to that taken in the conventional geometry (Fig. S4). Therefore, we advocate that the increased intensity at the wings does not arise from distinct Si species with discrete, core-shifted components, but is rather caused by the distribution of bond angles and bond lengths present at the strained interface. Finally, we note that in the work of Riedl *et al.*[11], both the *6R3* and “defect” components disappear upon H-decoupling of the buffer layer from the substrate, which is consistent with our interpretation of spectral broadening due to strained Si species.

Table S2: XSW results based on XPS peak-fitting models from Refs. [10] and [11]. Reported uncertainties are 1-sigma confidence bounds.

	Component, j	χ^2	P_j	z_j (Å)	f_j	σ_j (Å)
C 1s	Bulk C	1.30	0.76±0.03	2.39±0.13	0.85±0.1	0.23 ^{+0.07} _{-0.10}
	EG + S ₁	1.53	0.39±0.03	N/A	0.22±0.03	N/A
	S ₂	2.94	0.83±0.04	2.09±0.10	0.65±0.15	0.37 ^{+0.10} _{-0.07}
Si 1s	Bulk Si	4.85	1.00±0.02	2.52±0.05	0.88±0.08	0.21 ^{+0.06} _{-0.1}
	Si _{6R3}	2.15	0.95±0.06	2.42±0.13	0.9±0.3	0.18 ^{+0.12} _{-0.08}
	Si _{def}	0.79	0.97±0.11	2.44±0.25	0.6±0.3	0.4 ^{+0.2} _{-0.2}

Regardless, we are not limited in the analysis of a single peak fitting model, and therefore provide alternate XSW analysis using the XPS models offered by Emtsev and Riedl. The C 1s and Si 1s spectra fit according to these models in shown in Fig. S6. Both spectra are well fit based on the literature values. We note that in Emtsev's model, the S₁ and EG components differ in binding energy by only ~0.1 eV. This results in a high degree of covariance of peak fitting parameters for these two species, greatly complicating the XSW analysis. The S₂ component, on the other hand, is practically isolated (core-shifted by +1.1 eV) and can be analyzed in a straightforward manner. The XSW data and fits are presented in Figs. S6(b) and (c), and the results are summarized in Table S2. Because direct analysis of the EG + S₁ component proves impractical (the one measured Fourier component possesses as many as 4 distinct contributions), we explore Emtsev's model by constraining the S₂ species within its XSW-derived 1-sigma confidence window ($2.0 \text{ Å} < z_{S_2} < 2.2 \text{ Å}$, see Table S2) and mapping the goodness-of-fit χ^2 and R -factor as a function of z_{S_1} between $0.5 > z_{S_1} > 3.0$. The resulting χ^2 and R -factor maps are shown in Figure S7. There exist two distinct local minima in the map, indicating potential solutions for Emtsev's model at $z_{S_1} \sim 0.9 \text{ Å}$ and $z_{S_1} \sim 2.4 \text{ Å}$. The $z_{S_1} \sim 0.9 \text{ Å}$ solution would indicate Si-C and graphene-like C-C bonding distances that are incompatible with the interpretation of a partially-

bound graphene-like interfacial layer. The $z_{S_1} \sim 2.4 \text{ \AA}$ solution produces a structure largely similar to the one presented in the main text, but places the Si-C-C₃ bonded atoms at distances much larger than typical Si-C bond lengths. Furthermore, this model places the Si-C-C₃ bonded C atoms in a highly unphysical bonding geometry, at 0.3 \AA *above* the atoms in a graphene-like configuration.

The XSW modulations resulting from the fitting of the Si 1s spectra with distinct, core-shifted, non-bulk-like components are shown in Figure S6(d). The Fourier amplitudes and phases for these three components are practically indistinguishable within error (Table S2), indicating all species have similar positions and distributions with respect to the substrate lattice. While it is possible that this result indicates the existence of small populations (<5% at surface) of distinct chemical species positioned in bulk-like SiC positions, we would expect some non-bulk like XSW modulation of the Si 1s spectral components if any Si-Si bonds were present, and none is observed. An alternate explanation, in which interfacial strain causes increased variance in the distribution of Si-C bond lengths and angles of the topmost Si layers, thereby broadening the Si 1s spectral distribution, is more plausible.

Analysis of 0.5 ML UHV-grown 1.7 ML Ar-grown EG/SiC(0001):

C 1s and Si 1s spectra taken with emission angle $\alpha = 2^\circ$ are shown in Fig. S8 for both 0.5 ML UHV-grown [S8(a)-(b)] and 1.7 ML Ar-grown [S8(c)-(d)] EG/SiC(0001). Both samples exhibit C 1s spectra typical of EG/SiC(0001), but both Si 1s spectra also possess a strong high-BE component consistent with SiO_x chemical species [16]. This signal is only discernible when using the $\alpha = 2^\circ$ geometry, indicating that it is associated with a surface oxide species. Due to the relatively low spectral resolution of our measurement, we do not attempt to identify sub-oxide

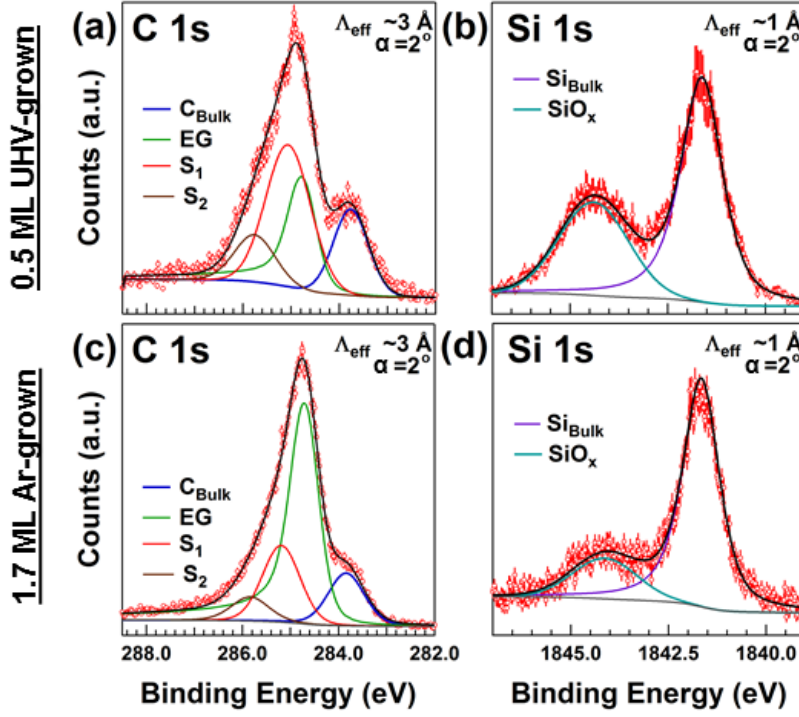


Figure S8: C 1s and Si 1s spectra from 0.5 ML (a)-(b) UHV-grown EG/SiC(0001) and (c)-(d) 1.7 ML Ar-grown EG/SiC(0001).

Table S3: XSW results for 0.5 UHV-grown and 1.7 ML Ar-grown graphene.

UHV-grown 0.5 ML EG/SiC(0001)					
Component, <i>s</i>	χ^2	P_s	z_s (Å)	f_s	σ_s (Å)
Bulk Si	2.12	0.99±0.01	2.49±0.03	0.90±0.03	0.18 ^{+0.03} _{-0.03}
SiO _x	2.03	N/A	N/A	0.1±0.1	N/A
Bulk C	6.22	0.74±0.02	1.87±0.05	0.95±0.08	0.1 ^{+0.07} _{-0.1}
S ₁	1.36	0.9±0.1	2.3±0.2	0.3±0.2	0.6 ^{+0.2} _{-0.2}
S ₂	1.21	0.8±0.05	2.0±0.1	0.9±0.2	0.18 ^{+0.15} _{-0.13}
EG	1.45	0.27±0.04	N/A	0.70±0.3	N/A
Ar-grown 1.7 ML EG/SiC(0001)					
Component, <i>s</i>	χ^2	P_s	z_s (Å)	f_s	σ_s (Å)
Bulk Si	0.33	1.00±0.01	2.52±0.03	0.94±0.08	0.1 ^{+0.07} _{-0.1}
SiO _x	1.09	N/A	N/A	0.0 ^{+0.2} _{-0.0}	N/A
Bulk C	3.37	0.74±0.02	1.87±0.05	0.86±0.07	0.22 ^{+0.06} _{-0.06}
S ₁	3.11	1.00±0.05	2.52±0.13	0.3±0.1	0.6 ^{+0.1} _{-0.05}
S ₂	0.86	0.84±0.03	2.12±0.07	1.00±0.14	0.1 ^{+0.07} _{-0.1}
EG	1.21	0.34±0.04	N/A	0.52±0.09	N/A

signals within the Si 1s, as have been observed previously [16]. We do note, however, that in the case of the 1.7 ML sample, which has a weaker oxide signal, the SiO_x core-level shift is 0.3 eV less than that of the 0.5 ML sample, suggesting increased contribution from lower-BE sub-oxide species. The oxygen concentration can be estimated by comparing the integrated O 1s signal intensity to that of the EG C 1s signal. The density of C in EG form is estimated from the unit cell definition to be 38.2 C/nm², and therefore, by correcting for the relative C and O photoionization cross-sections at ~2.5 keV, we estimate a concentration of ~2 O/nm² for the 1.7 ML Ar-grown sample, and ~6 O/nm² for the 0.5 ML UHV-grown sample. For the Ar-grown sample, the oxide formation may be caused by the presence of trace O₂ or H₂O in the chamber during growth or cool down. In the case of the UHV-grown sample the oxide formation may arise due to exposure of the more reactive sub-ML sample, which has large regions of exposed zero-layer graphene, to air.

XSW results for both samples are shown in Fig. S9, and the results are summarized in Table S3. The most notable result is that for the Si_{Bulk}, C_{Bulk}, S₁ and S₂ values are essentially identical between all measured samples. Considering that these samples were made using different growth methods, in different laboratories, and possess differing EG and oxide coverage, these nearly identical results are a testament to the ubiquity of the interfacial structure. The SiO_x components are randomly distributed, indicating that there exists a thick or broadly distributed (as opposed to single oxide monolayer) region of silicon oxide near the SiC surface. The 0.5 ML UHV-grown EG result is interesting as it approaches the value expected for mainly monolayer graphene (at $z_{EG_1} \sim 5.8$ Å, an isolated monolayer would give a coherent position of $P_{EG_1} = 0.30$). This, along with the relatively high measured coherent fraction ($f_{EG} = 0.7 \pm 0.3$), indicates that most of the EG signal originates from monolayer graphene. Contribution from the second layer

of EG, EG₂ (at $z_{\text{EG}_2} \sim 9.15 \text{ \AA}$) would, in principle, shift the Fourier phase positive and reduce the coherent fraction, as is observed for samples with higher EG coverage. It should be noted that the XSW-XPS data for the 0.5 ML sample possess poorer counting statistics, which is reflected in the generally larger degree of scatter in the data and uncertainty values in the extracted XSW results.

The 1.7 ML Ar-grown sample serves to validate the XSW-XRR analysis performed in the main text. Qualitatively, the XSW values for S₁ and S₂ agree extremely well with those in the main text (within 1-sigma in both cases), indicating that the two samples have essentially

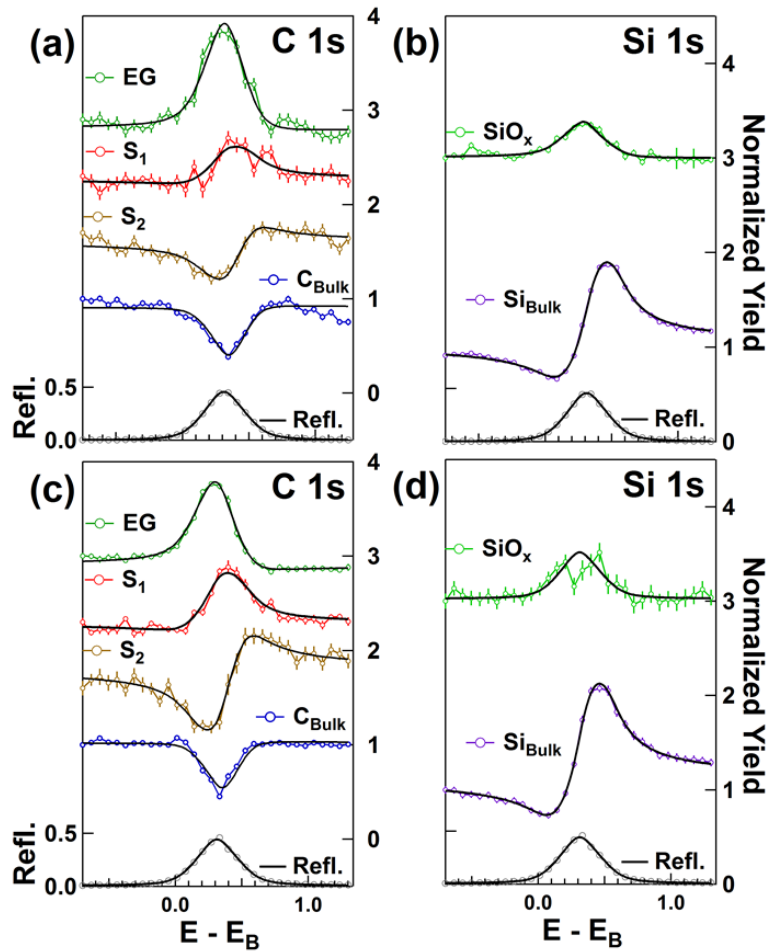


FIG. S7: XSW results for (a) C 1s 0.5 ML UHV-grown. (b) Si 1s 0.5 ML UHV-grown. (c) C 1s 1.7 ML furnace-grown. (d) Si 1s 1.7 ML UHV-grown EG/SiC(0001) samples.

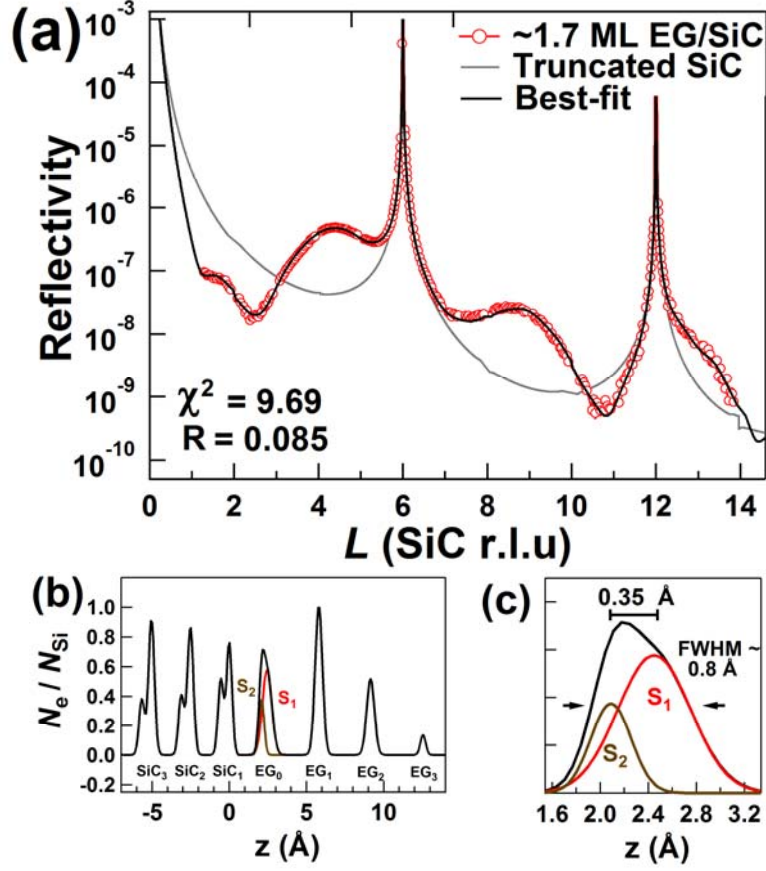


FIG S8: XRR analysis for the 1.7ML Furnace-grown EG/SiC(0001) sample. Results are highly comparable to those found in the main text, apart from a higher degree of graphene coverage.

identical interfacial structure. The differing XSW result for the EG component is due to the varying amount of EG coverage on the samples. The XRR data and XSW-constrained best-fit result is shown in Fig. S10. We find that the values $z_{EG_1} \sim 5.80$ Å, $z_{EG_2} \sim 9.15$ Å, and $z_{EG_3} \sim 12.55$ Å yield $\chi^2 = 9.69$ and R -factor = 0.085, comparable to values found for 1.3 ML EG/SiC(0001) of $\chi^2 = 7.19$ and R -factor = 0.079. The slightly poorer quality of the fit for the Ar-grown sample may be attributed to the inability to accurately model the contribution of the SiO_x in the electron density profile. Relative layer coverages were $c_{EG_1} \sim 1.00$ ML, $c_{EG_2} \sim 0.55$ ML, and $c_{EG_3} \sim 0.10$ ML, summing to a total coverage of 1.7 ML. The back-calculation of the XSW values gives $f_{EG} = 0.38$ and $P_{EG} = 0.44$, near the 1-sigma of the uncertainty limits for XSW results reported in Table

S3. In all, the consistency across sample coverage, production method, and sample morphology provides strong support for conclusions stated in the main text.

- [1] J. Zegenhagen, B. Detlefs, T.L. Lee, S. Thiess, H. Isern, L. Petit, L. Andre, J. Roy, Y.Y. Mi, I. Jourard. "X-ray standing waves and hard X-ray photoelectron spectroscopy at the insertion device beamline ID32," *Journal of Electron Spectroscopy and Related Phenomena* **178**, 258-267 (2010).
- [2] J.J. Lee, C.J. Fisher, D.P. Woodruff, M.G. Roper, R.G. Jones, B.C.C. Cowie. "Non-dipole effects in photoelectron-monitored X-ray standing wave experiments: characterisation and calibration," *Surface Science* **494**(3), 166-182 (2001).
- [3] I.A. Vartanyants, J. Zegenhagen. "Quadrupole contribution to the angular resolved photoemission from an X-ray interference field," *Physica Status Solidi B-Basic Research* **215**(1), 819-826 (1999).
- [4] P. Fenter, J.G. Catalano, C. Park, Z. Zhang. "On the use of CCD area detectors for high-resolution specular X-ray reflectivity," *Journal of Synchrotron Radiation* **13**, 293-303 (2006).
- [5] J.D. Emery, Q.H. Wang, M. Zarrouati, P. Fenter, M.C. Hersam, M.J. Bedzyk. "Structural analysis of PTCDA monolayers on epitaxial graphene with ultra-high vacuum scanning tunneling microscopy and high-resolution X-ray reflectivity," *Surface Science* **605**(17–18), 1685-1693 (2011).
- [6] G.K. Wertheim. "Deconvolution and smoothing: Applications in ESCA," *Journal of Electron Spectroscopy and Related Phenomena* **6**(3), 239-251 (1975).
- [7] S. Doniach, M. Sunjic. "Many-electron singularity in X-ray photoemission and X-ray line spectra from metals," *Journal of Physics Part C Solid State Physics* **3**(2), 285 (1970).
- [8] D.A. Shirley. "High-resolution X-ray photoemission spectrum of the valence bands of gold," *Physical Review B* **5**(12), 4709 (1972).
- [9] J.D. Emery, V.D. Wheeler, B. Detlefs, M.E. McBriarty, S.S. Lee, P. Fenter, J. Zegenhagen, D.K. Gaskill, M.J. Bedzyk. "Interfacial Structure of H-intercalated Epitaxial Graphene on SiC(0001)," In Preparation, (2013).
- [10] K.V. Emtsev, F. Speck, T. Seyller, L. Ley, J.D. Riley. "Interaction, growth, and ordering of epitaxial graphene on SiC{0001} surfaces: A comparative photoelectron spectroscopy study," *Physical Review B* **77**(15), 155303 (2008).

- [11] C. Riedl, C. Coletti, T. Iwasaki, A.A. Zakharov, U. Starke. "Quasi-free-standing epitaxial graphene on SiC obtained by hydrogen intercalation," *Physical Review Letters* **103**(24), 246804 (2009).
- [12] C. Riedl, U. Starke, J. Bernhardt, M. Franke, K. Heinz. "Structural properties of the graphene-SiC(0001) interface as a key for the preparation of homogeneous large-terrace graphene surfaces," *Physical Review B* **76**(24), 374009 (2007).
- [13] S. Forti, K.V. Emtsev, C. Coletti, A.A. Zakharov, C. Riedl, U. Starke. "Large-area homogeneous quasifree standing epitaxial graphene on SiC(0001): Electronic and structural characterization," *Physical Review B* **84**(12), 125449 (2011).
- [14] S. Goler, C. Coletti, V. Piazza, P. Pingue, F. Colangelo, V. Pellegrini, K.V. Emtsev, S. Forti, U. Starke, F. Beltram. "Revealing the atomic structure of the buffer layer between SiC (0001) and epitaxial graphene," *Carbon* **51**, 249-254 (2012).
- [15] K.V. Emtsev, A. Bostwick, K. Horn, J. Jobst, G.L. Kellogg, L. Ley, J.L. McChesney, T. Ohta, S.A. Reshanov, J. Rohrl, *et al.* "Towards wafer-size graphene layers by atmospheric pressure graphitization of silicon carbide," *Nature Materials* **8**(3), 203-207 (2009).
- [16] L.I. Johansson, C. Virojanadara, T. Eickhoff, W. Drube. "Properties of the SiO₂/SiC interface investigated by angle resolved studies of the Si 2p and Si 1s levels and the Si KLL Auger transitions," *Surface Science* **529**(3), 515-526 (2003).